Optimization of hepatic vasculature segmentation from contrast-enhanced MRI, exploring two 3D Unet modifications and various loss functions

Ivashchenko, Oleksandra, Zhai, Zhiwei, Stoel, Berend, Ruers, Theo J.

Oleksandra V. Ivashchenko, Zhiwei Zhai, Berend C. Stoel, Theo J. M. Ruers, "Optimization of hepatic vasculature segmentation from contrast-enhanced MRI, exploring two 3D Unet modifications and various loss functions," Proc. SPIE 11598, Medical Imaging 2021: Image-Guided Procedures, Robotic Interventions, and Modeling, 115980J (15 February 2021); doi: 10.1117/12.2574267

SPIE.

Event: SPIE Medical Imaging, 2021, Online Only

Optimization of hepatic vasculature segmentation from contrast-enhanced MRI, exploring two 3D Unet modifications and various loss functions

Oleksandra V. Ivashchenko*[§a,b], Zhiwei Zhai[§a], Berend C. Stoel[a], Theo J.M. Ruers[b,c]
[a] Department of Radiology, Leiden University Medical center, Albinusdreef 2, 2333ZA Leiden, The Netherlands; [b] Department of Surgical Oncology, The Netherlands Cancer Institute Antoni an Leuwenhoek Hospital, Plesmanlaan 121, 1066CX Amsterdam, The Netherlands; [c] Nanobiophysics Group, Faculty of Science and Technology, University of Twente, Drienerlolaan 5, 7522 NB Enschede, The Netherlands.

ABSTRACT

Although MRI with hepatospecific contrast agents is a new standard diagnostic imaging for patients with liver cancer, there are no automated methods for detailed segmentation of the liver vasculature in cases with progressed tumors. This is due to the anatomical complexity, underlying disease and tunability of MRI image contrast, which challenge automatization. Here, we investigated the feasibility of liver vessel segmentation with three CNN architectures in combination with four different loss functions. In particular, a 3D Unet, a Vnet and its modification with an intra-layer dense block (DVnet) were evaluated. Dice-based loss, categorical cross entropy (CCE), weighed categorical cross entropy (WCCE) and focal loss (FL) were used as loss functions for training, the latter two to deal with the imbalanced class problem. A cohort of 90 patients (60 training, 10 validation and 20 testing) with progressed liver tumors were involved in this study, with manually annotated liver vasculature as a "gold standard". Trained networks were evaluated by means of the Dice coefficient and centerline-based F1 score calculations. Models trained with balanced loss functions (FL,WCEE) performed the best for DVnet, while Vnet had the best performance for unbalanced loss functions. Vnet and DVnet architectures trained with an FL had the best overall segmentation accuracy (DC = 70%), while networks with a Dice-based loss had the lowest performance (max DC = 42%). In conclusion, the use of balanced loss functions, addition of an intra-layer dense block and drop-outs into the network architecture improved handling the unbalanced class problem in liver vessel segmentation.

Keywords: vessel segmentation, 3D Unet, Vnet, loss function, liver anatomy, MRI segmentation, surgical planning.

1. INTRODUCTION

Liver tumors, either from primary liver cancer or metastatic disease, pose a significant health burden worldwide, with over 1.7 million new cases in 2018 [1], [2]. Although treatment for liver tumors can include radiofrequency or microwave ablation, surgery, radio- or chemotherapy, as well as a combination of the aforementioned techniques, surgery still provides the best prognosis to the patient and is the only technique that can even offer curation [3]. However, even in the case of localized disease, planning of the resection is challenging. This may be partially due to the presence of an underlying liver disease, yet mainly because of the complexity of the organ's anatomy and increasing complexity of the resections in the last years (i.e., acceptable number of lesions per patient and more challenging locations within the organ). As a result, the use of patient-specific 3D models of liver anatomy that includes the underlying vasculature has become widely accepted for preparation and safe execution of surgical resections [4], [5]. The necessity of such models even increases with the

*o.ivashchenko@lumc.nl; phone 31 071 526 3979
§ equal contribution

Medical Imaging 2021: Image-Guided Procedures, Robotic Interventions, and Modeling,
edited by Cristian A. Linte, Jeffrey H. Siewerdsen, Proc. of SPIE Vol. 11598, 115980J

rapid increase in the number of liver resections performed under image guidance (e.g., navigated procedures), which require intraoperative co-registration of the preoperative model and the intraoperative imaging (i.e., ultrasound).

Nowadays, 3D models of hepatic vasculature can be, for example, fully automatically extracted from contrast-enhanced abdominal Computed Tomography (CT) scans. Although there are various CT-based techniques that provide high segmentation accuracy and detailed 3D models of liver anatomy, this imaging modality is no longer the preferred diagnostic imaging for detection of liver lesions and surgical planning [6]–[8], and was replaced by Magnetic Resonance Imaging (MRI). This is due to the fact that MRI, in particular with hepatospecific contrast agents [7], [9], provides significantly higher sensitivity and specificity for lesion detection, also results in better visualization of the complete underlying vascular and biliary anatomy. These properties turn MRI into a perfect candidate for diagnostic imaging and planning tool for complex image-guided liver resection. However, to date, there is no robust method of hepatic vasculature segmentation from these MRI scans. Additionally, methods developed so far were not trained or tested on patient data with progressed liver cancer, where image quality is often significantly impaired by the underlying liver disease and multiple lesions. Unlike with CT, segmentation methods developed for MRI scans acquired with a very dedicated imaging sequence (i.e., angiography, DWI, SPIR, BOLD), cannot be directly translated to an alternative acquisition type. As a result, although several groups have previously published respected results on MRI-based segmentation [10]–[12], only few of them can be used for vessel segmentation in metastatic livers acquired with generic diagnostic MRI sequences (i.e., T1-mDIXON, TSE, SE).

In this work, we investigated the feasibility of hepatic vasculature segmentation with various 3D Unet-like architectures. In particular, we explored the influence of various architecture modifications (e.g., dilated convolution, dense block addition, drop-outs) and loss functions (e.g., Dice, cross-entropy, focal loss) on the performance of the segmentation. Our goal was to develop a method that is able to segment hepatic vasculature from liver MRI scans with hepatospecific contrast agents, because currently they are used as a pre-treatment imaging for patients with liver tumors. Therefore, the network will need to learn not only a typical vasculature anatomy, but also the distinction between vessel-to-tumor or vessel-to-previous treatment artifact (i.e., ablation zones) borders. The networks are trained and evaluated using a cohort of 90 MRI liver scans, each containing multiple tumors and old ablation zones.

2. METHODS

2.1 Data acquisition

With approval of the Medical Ethical Committee of the Netherlands Cancer Institute Antoni van Leeuwenhoek Hospital (NKI-AvL) and under a Data transfer agreement with the Leiden University Medical Center (LUMC), a total of 90 contrast-enhanced liver MRI scans of the NKI-AvL patients were retrospectively selected. The full list of patient inclusion criteria is provided in Table 1. The MRI acquisition used in this work is a 10ml Gd-EOB-DTPA (Primovist, Bayer AG, Germany) enhanced mDIXON sequence, a standard anatomical acquisition technique. This hepatospecific contrast agent initially distributes in the extracellular fluid compartment (i.e., standard arterial and venous phase), yet is actively taken up by the hepatocytes, thus is excreted into the bile. As a result, it allows visualizing the complete hepatic and biliary anatomy in one dynamic scan. This, together with superior sensitivity and specificity of the agent for detection of liver tumors, as compared to CT [8], is the main reason why it is standardly used for diagnostic and treatment planning of liver malignancies. The total acquisition protocol consists of five dynamic phases: 10s, 25s, 1 min, 3 min and 20 min post injection of the contrast agent. Only a 20 min post injection phase was used in this work. Each phase is acquired with a T1-weighted 3D Fast Field Echo 2-point mDIXON single breath-hold scan in expiration, acquired on a 1.5 or 3.0T Philips Achieva scanner. Reconstruction voxel grid of 1.0 x 1.0 x 1.5 mm, with a FOV of 400 x 300 x 230 mm (RL/AP/FH), TE1/TE2/TR of 1.13/2.2 /3.5ms, SENSE factors of 2.4/1.5 (AP/FH), and a half-scan factor of 0.875 in two directions were used. No further post-processing, filtering or resampling of the data was applied.

Table 1. Patient inclusion criteria.

Parameter	Value
MRI scan type	Multi-phase Gd-EOB-DTPA
MRI image quality requirements	No or minor motion artifacts
Age	> 18, no upper limit
Tumor type	No restriction on histology of the tumor
Tumor size	2 to 15 cm
Number of tumors within the liver	1 to 15 tumors

2.2 Pre-processing and data annotation

In order to generate a "gold standard" segmentation, each MRI scan was manually annotated by an expert user (i.e., responsible for preparation of patient-specific 3D models at the NKI-AvL) using the 3D Slicer open source software [13], [14]. Three types of anatomical structures were specified: liver contour, hepatic and portal veins. After this, each scan was cropped with a bounding box surrounding the liver mask. To minimize inter-patient variability and tunability of the MRI contrast, the intensity of the scan was normalized. Absolute intensity range of the late MRI phase is predominantly determines by patient-specific uptake of the contrast in the liver. Therefore, efficient normalization of the image requires consideration of liver intensity only. Normalization was performed by subtracting the average intensity and dividing by the standard deviation of MRI volume intensity within the liver mask region, as described in the equation (1)

$$I_{norm} = \frac{I_{orig} - \mu}{\sigma} \tag{1}$$

where I_{orig} is the original MRI image, I_{norm} is normalized image, μ and σ is the average and standard deviation intensity within liver mask region.

2.3 Deep learning architecture, loss function and training

A Vnet architecture with dilated convolution and residual dense block strategy (i.e., DVnet) was adapted for liver vein segmentation (Figure 1). The architecture consists of an encoder, which includes 4 layers of down-sampling, and a decoder which is comprised of 4 up-sampling layers. The dense block with residual mechanism is applied in each down / up-sampling layer. A 3D residual Unet with multi-scale supervision, and a Vnet were used for comparison [15], [16].

Liver vein segmentation is a typical imbalanced class problem, as the ratio between veins and background is extremely low. To deal with this imbalance, we adapted two balanced loss functions: the focal loss (FL) [17] and a weighted categorical cross entropy (WCCE). Dice-based loss and categorical cross entropy (CCE) were used for comparison. The focal loss was calculated as follows:

$$FL(p_c) = -\alpha(1 - p_c)^{\gamma} \log(p_c) \tag{2}$$

where α is a balanced parameter and γ is a focusing parameter. The WCCE loss function can be obtained from the FL definition in equation 2, by setting γ to 0; while CCE is obtained by setting α to 1 and γ to 0.

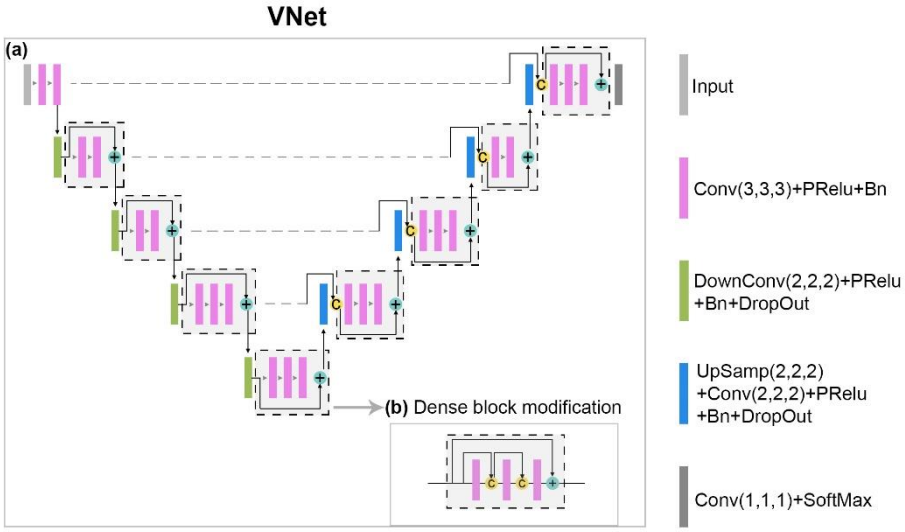

Figure 1. (a) Schematic representation of the Vnet architecture used in this work. Dashed boxes indicate sections of the Vnet that contains a dense block modification in the DVnet architecture. An example of a typical dense block modification is illustrated in (b).

3. EXPERIMENTS AND RESULTS

Twelve combinations of architectures and loss functions were trained in this work. The dataset consisted of 90 patients with liver lesions: 70 during training (60 for training, 10 for validation) and 20 during quantitative evaluation of the fully trained models (i.e., testing set). The testing data was randomly selected to represent a broad patient population; therefore it included six cases with previous liver resections, eight cases with previous RFA ablations of central lesions, and six cases that had no previous liver interventions. Each network was trained using a batch size of 10, and 3D patches with size 64x64x32 pixels, which were extracted from the normalized MRI scans, corresponding to a 64x64x48 mm volume (i.e., 7 - 10 % of the liver volume). Random patch generation strategy was used for training; Adam was used as optimizer, with a maximum of 120 epochs. An initial learning rate of 1e-3 was used, with a reduction factor 0.5 and a minimum learning rate of 1e-5. For all FL models α and γ were set to 0.8 and 2.0, respectively. The influence of varying α and γ weight factors on the performance of CNN's trained with a focal loss or a WCCE was extensively evaluated in Lin et.al. [17], where these loss functions were introduces and evaluated. Lin et al. stated that models trained with α=0.8 and γ=2.0 result in the best performance for unbalanced class problems (e.g., vasculature segmentation). Validity of this statement was qualitatively evaluated at the beginning of our project, and our initial results supported Lin et.al. Therefore, both weight factors were fixed to the aforementioned values.

After training the CNNs, an additional quantitative evaluation of the segmentation accuracy with respect to the "gold standard" was performed using 20 test datasets. For each of the twelve combinations of CNN architecture and loss function, the following accuracy metrics were calculated: Dice coefficient (DC) for each vessel type, the DC for the entire vasculature and F1 score based on vessel centerlines. During F1 score calculation, vessel centerlines of the "gold standard" and automated segmentations were extracted with a distance transform method [18]. Next, the F1 score was calculated using the true positive (TP) rate, corresponding to voxels of hepatic vasculature located within one vessel diameter distance from the "gold standard" centerline; false positive (FP) rate was the total number of voxels in the test dataset segmentation minus the TP; false negative (FN) rate was the "gold standard" minus the TP fraction (see Table 2).

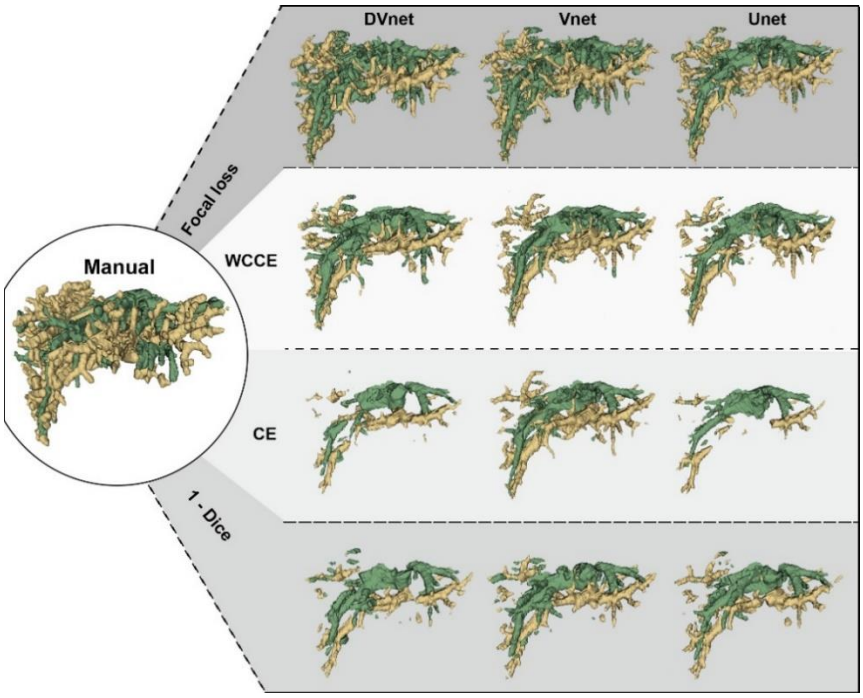

Figure 2. Rendering of hepatic vessel segmentation achieved with a manual segmentation (center), DVnet, Vnet and 3D Unet CNN architectures with a Dice based-loss, CCE, WCCE, and FL, respectively.

According to the DC for the complete vasculature, hepatic and portal veins, the DVnet architecture with FL function resulted in the best liver vessel extraction, and Vnet architecture with FL obtained comparable results (DC = 69.5±7.4 and 69.6±7.2, respectively). All models trained with balanced loss functions (i.e., FL and WCCE) had the best performance for DVnet architecture, followed by Vnet and 3D Unet, respectively. In contrast, models trained with unbalanced loss functions (i.e., CCE and 1-Dice) had nearly comparable performance for Vnet and 3D Unet architectures (slight outperformance of 3D Unet), while DVnet was lagging behind.

Considering the complexity of testing MRI cases, we additionally measured the inter-observer variability of manual segmentations. This was done by measuring the DC between manual segmentations performed by an additional user, with respect to the reference "gold standard" manual segmentation of the expert user, used as a benchmark in the study. These segmentations did not exceed DC of 78.4 (complete vasculature), when compared to the "gold standard" segmentation.

The quality of the testing results can be assessed visually in Figures 2-4. In Figure 2, a 3D rendering is presented of the final segmentation results achieved with all network architectures and loss function combinations for one of twenty testing datasets. In Figure 3 and 4, axial MRI slices with color-coded contours of the manual and automatic segmentations with each of the 12 models are showed, corresponding to segmentation results achieved with MRI datasets corresponding to challenging anatomy (Figure 3), as well as those representing a "typical" clinical data (Figure 4).

Table 2. Quantitative comparison of the segmentation, median (IQR). The best performing CNN for each loss function type is highlighted in bold.

CNN type	Loss Function	Segmentation time (s)	DC (all veins)	DC (hepatic vein)	DC (portal vein)	F1 (all veins)
DVnet	1-Dice	62.5	35.9 (9.5)	43.4 (12.1)	25.6 (6.7)	0.44 (0.12)
	CCE	-	32.9 (12.6)	41.7 (10.4)	23.4 (8.0)	0.35 (0.14)
	WCCE	-	60.8 (8.2)	53.9 (6.5)	53.9 (9.7)	0.69 (0.12)
	FL	60.9	**69.5 (7.4)**	**64.7 (5.0)**	**60.3 (8.4)**	0.77 (0.09)
Vnet	1-Dice	59.4	41.6 (11.7)	51.1 (5.1)	28.9 (9.4)	0.49 (0.14)
	CCE	-	48.8 (9.9)	51.2 (7.0)	42.1 (8.6)	0.56 (0.15)
	WCCE	-	52.8 (11.5)	55.4 (8.4)	43.1 (8.8)	0.67 (0.13)
	FL	59.6	**69.6 (7.2)**	63.7 (7.6)	**60.3 (7.7)**	**0.80 (0.06)**
3D Unet	1-Dice	77.9	39.1 (7.1)	46.7 (10.0)	29.1 (7.9)	0.44 (0.12)
	CCE	-	22.4 (4.5)	31.5 (7.1)	13.8 (7.0)	0.29 (0.08)
	WCCE	-	43.9 (9.6)	52.8 (9.1)	32.3 (9.0)	0.54 (0.13)
	FL	58.3	55.1 (8.6)	53.5 (5.3)	43.8 (8.7)	0.66 (0.10)

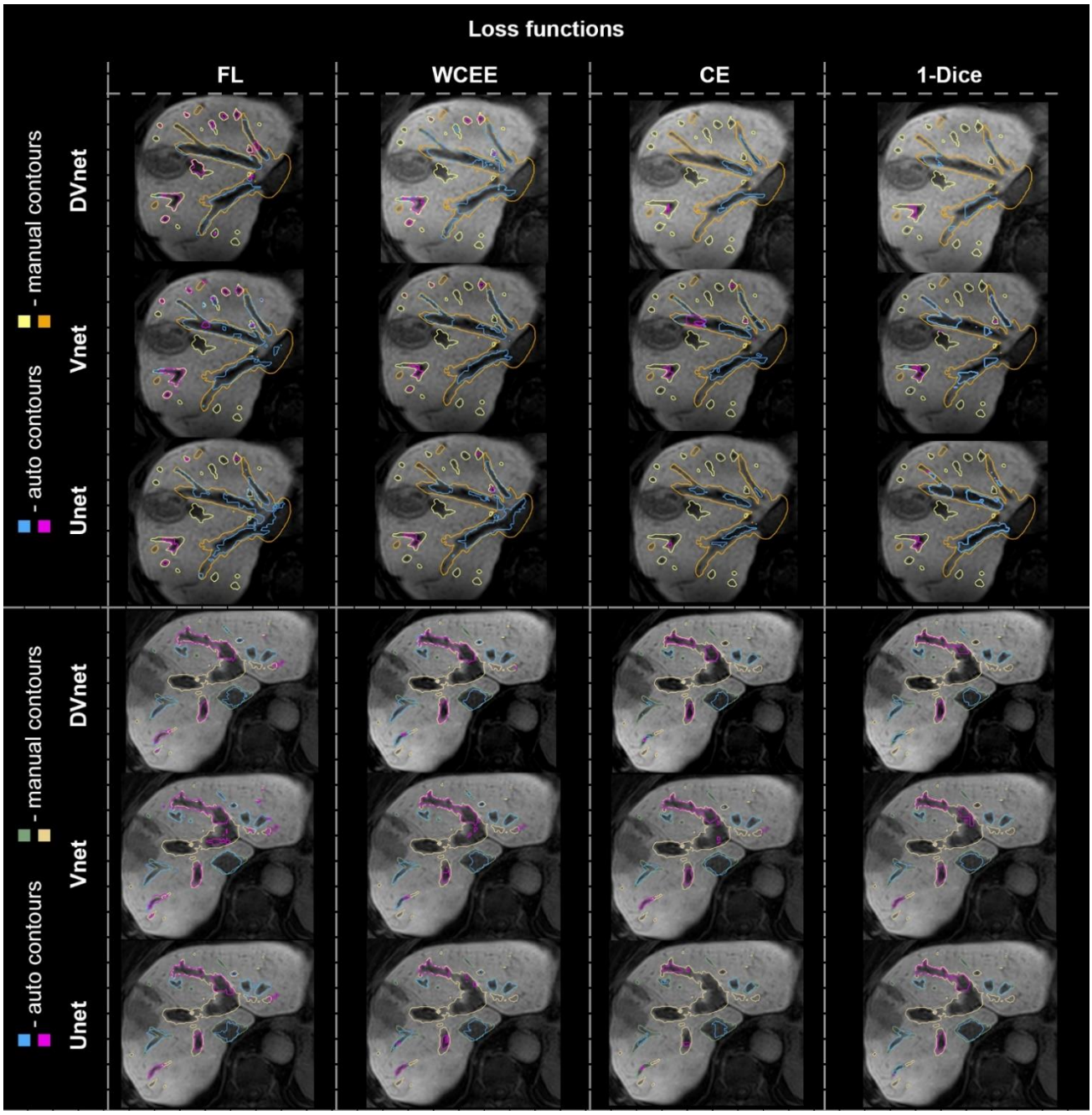

Figure 3. Visual comparison of final segmentation contours, achieved with each trained model, compared to the "gold standard" manual segmentations for two MRI test datasets, containing challenging anatomy of the liver (e.g., high tumor load).

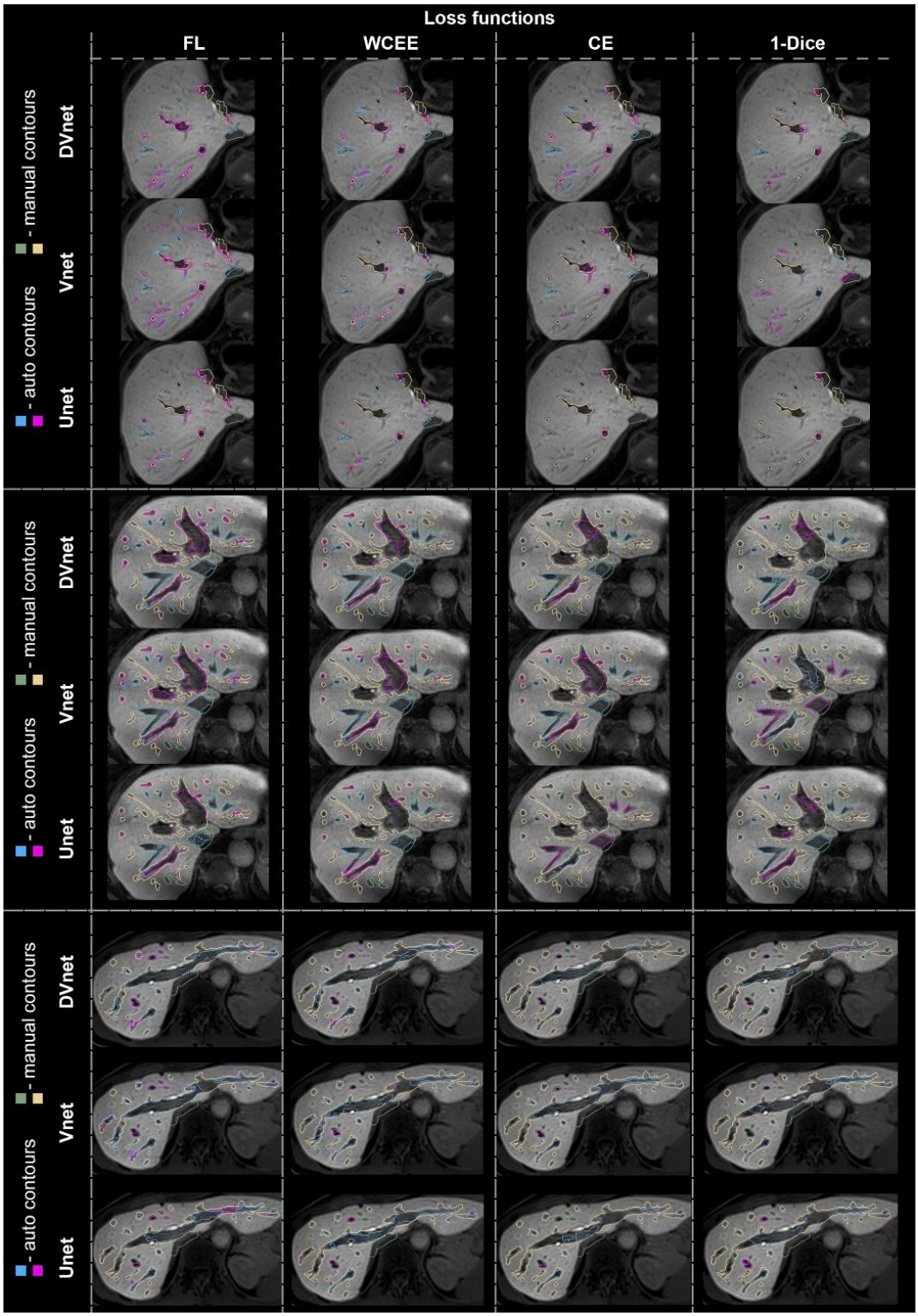

Figure 4. Visual comparison of final segmentation contours, achieved with each trained model, compared to the "gold standard" manual segmentations for three MRI test datasets, containing typical anatomy of the liver.

4. DISCUSSION

In this work, we investigated the feasibility of automated liver vessel segmentation from MRI scans of patients with progressed liver cancer, using the combination of three CNN architectures and four loss functions. In particular, 3D Unet, Vnet and its modification with an intra-layer dense block (DVnet) were evaluated. Each network architecture and loss function combination was trained and quantitatively tested with respect to the manually annotated "gold standard". According to the Dice metrics, networks trained with an FL loss function performed better than those trained with a WCCE, CCE and 1-Dice lose functions (Table 1). Therefore, our results suggest that focal loss is better at handling the imbalanced class problem (i.e., liver vessels) and, thus, works better than CCE even with balanced weights. When looking at different deep learning architectures, addition of the dense block slightly improved detection of liver vessels, though this difference was not statistically significant. Additionally, centerline based F1-score calculation showed that Vnet (FL) slightly outperformed DVnet (FL). At the same time, considering that DVnet (FL) achieved higher Dice scores, DVnet architecture might be better at the vessel edge detection.

The highest segmentation accuracy reached in this work did not exceed a DC of 70.0, which may be interpreted as a low segmentation accuracy. However, we want to stress that already inter-observer variability of expert manual segmentations was as high as 21%. Therefore, the low DC is confounded by bias in the vessel-to-tumor border and vessel edge definition in manual segmentations. The later challenge is directly related to tunable contrast and contrast gradients in MRI data.

Although the Dice-based loss function did not result in the best overall performance, it was better than the two unbalanced loss functions tested within this work. Unlike with balanced loss functions (i.e., FL, WCCE), where DVnet outperformed Vnet and 3D Unet, respectively, Vnet provided the best results for unbalanced loss functions. Here, performance difference between the Vnet and 3D Unet is directly related to effects of the drop-outs, which were used in every layer of the Vnet.

The main weakness of the DVnet model trained with a FL loss function is related to its poor segmentation performance near the portal bifurcation into the left and right portal vein. Similar challenges were observed in all network models evaluated in this work. The central portal vein bifurcation is located near the posterior-caudal surface of the liver, and is a non-enhanced vessel in the delayed MRI phase (i.e., input scan for the segmentation), also has low visibility with respect to the organ's surrounding. Moreover, the portal bifurcation has two different edge contrast gradient in the direction of the liver parenchyma (i.e., strong negative contrast) and the bowels (i.e., weak positive), which additionally challenges detection of the vessel. We expect that it may be possible to address this challenge by incorporation of targeted patch sampling of the portal vein and with help of attention learning [19], [20], which have already illustrated promising results for unbalanced segmentation challenges. However, further investigation of this topic will be covered in our future work.

To our knowledge, this is the first study that introduces high-accuracy MRI-based segmentation method for extraction of liver vessels from scans of patient with progressed liver tumors. The segmentation method was developed using widely accepted generic mDIXON sequence [21], which is frequently applied during abdominal MRI acquisitions, partially due its low sensitivity to inhomogeneities of the magnetic field [22]. The study data consisted of 1.5 and 3 Tesla datasets, to increase generalizability of trained models (e.g. scanner independency). Additionally, it was normalized with a patient-specific contrast uptake within the liver, to further suppress inter-dataset variability of the image quality (e.g. contrast, effective SNR). These design choices are expected to make the network less sensitive to various sequence- or scanner-specific image quality or organ appearance variations, and thus may improve applicability of the method. Liver surgeons at the NKI-AvL feel that segmentation results currently achieved with the DVnet warrants further clinical implementation as a planning tool for interventional procedures, generic liver resections, as well as to server as a guidance model for image-guided and robotically-assisted resections (e.g. navigated surgery).

REFERENCES

[1] WHO, "Globocan 2012 International Agency for Research on Cancer (IARC)," *2012*, vol. 876, p. 4, 2012.

[2] "Globocan 2018: World Health Organization, International Agency for Research on Cancer.," 2019.

[3] N. N. Keum and E. Giovannucci, "Global burden of colorectal cancer: emerging trends, risk factors and prevention strategies," *Nat. Rev. Gastroenterol. Hepatol.*, 2019.

[4] V. Ferrari *et al.*, "Value of multidetector computed tomography image segmentation for preoperative planning in general surgery," *Surg. Endosc.*, vol. 26, no. 3, pp. 616–626, 2012.

[5] E. Perica and Z. Sun, "Patient-specific three-dimensional printing for pre-surgical planning in hepatocellular carcinoma treatment," *Quant. Imaging Med. Surg.*, vol. 7, no. 6, pp. 668–677, 2017.

[6] A. Vogel *et al.*, "Hepatocellular carcinoma: ESMO Clinical Practice Guidelines for diagnosis, treatment and follow-up," *Ann. Oncol.*, vol. 29, no. Supplement 4, pp. iv238–iv255, 2018.

[7] A. Forner *et al.*, "Diagnosis of hepatic nodules 20 mm or smaller in cirrhosis: Prospective validation of the noninvasive diagnostic criteria for hepatocellular carcinoma," *Hepatology*, vol. 47, no. 1, pp. 97–104, 2008.

[8] Y. J. Lee *et al.*, "Hepatocellular carcinoma: Diagnostic performance of multidetector CT and MR imaging-a systematic review and meta-analysis," *Radiology*, vol. 275, no. 1, pp. 97–109, 2015.

[9] P. Reimer, G. Schneider, and W. Schima, "Hepatobiliary contrast agents for contrast-enhanced MRI of the liver: Properties, clinical development and applications," *Eur. Radiol.*, vol. 14, no. 4, pp. 559–578, 2004.

[10] M. Lebre, A. Vacavant, and M. Grand-brochier, "Automatic 3D skeleton-based segmentation of liver vessels from MRI and CT for couinaud representation," in *2018 25th IEEE International Conference on Image Processing (ICIP)*, 2018, pp. 3523–3527.

[11] M. A. Lebre *et al.*, "A robust multi-variability model based liver segmentation algorithm for CT-scan and MRI modalities," *Comput. Med. Imaging Graph.*, vol. 76, p. 101635, 2019.

[12] E. Goceri, Z. K. Shah, and M. N. Gurcan, "Vessel segmentation from abdominal magnetic resonance images: adaptive and reconstructive approach," *Int. j. numer. method. biomed. eng.*, vol. 33, no. 4, pp. 1–16, 2017.

[13] A. Fedorov *et al.*, "3D Slicer as an image computing platform for the Quantitative Imaging Network," *Magn. Reson. Imaging*, vol. 30, no. 9, pp. 1323–1341, 2012.

[14] O. Ivashchenko *et al.*, "Automated segmentation of the liver and hepatic vasculature, and biliary tree anatomy from multiphase MR images," *Magn. Reson. Imaging*, vol. 68, no. May, pp. 53–65, 2020.

[15] W. Yu, B. Fang, Y. Liu, M. Gao, S. Zheng, and Y. Wang, "Liver Vessels Segmentation Based on 3d Residual U-NET," in *2019 IEEE International Conference on Image Processing (ICIP)*, 2019, pp. 250–254.

[16] F. T. Ferreira, P. Sousa, A. Galdran, M. R. Sousa, and A. Campilho, "End-to-End Supervised Lung Lobe Segmentation," pp. 4763–4770, 2018.

[17] T. Y. Lin, P. Goyal, R. Girshick, K. He, and P. Dollar, "Focal Loss for Dense Object Detection," in *Proceedings of the IEEE International Conference on Computer Vision*, 2017, vol. 2017-Octob, pp. 2999–3007.

[18] C. W. Niblack, P. B. Gibbons, and D. W. Capson, "Generating skeletons and centerlines from the distance transform," *CVGIP Graph. Model. Image Process.*, vol. 54, no. 5, pp. 420–437, 1992.

[19] J. Schlemper *et al.*, "Attention-gated networks for improving ultrasound scan plane detection," *arXiv*, no. Midl, pp. 1–12, 2018.

[20] O. Oktay *et al.*, "Attention U-Net: Learning where to look for the pancreas," *arXiv*, no. Midl, 2018.

[21] Q. S. Xiang, "Two-point water-fat imaging with partially-opposed-phase (POP) acquisition: An asymmetric dixon method," *Magn. Reson. Med.*, vol. 56, no. 3, pp. 572–584, 2006.

[22] J. Ma, "Dixon techniques for water and fat imaging," *J. Magn. Reson. Imaging*, vol. 28, no. 3, pp. 543–558, 2008.